

Nonlinear fast magnetoacoustic wave interaction with 2D magnetic X-points in the ion cyclotron range of frequencies

J. W. Threlfall¹, C. E. Parnell¹, I. De Moortel¹, K. G. McClements², and T. D. Arber³

¹ School of Mathematics and Statistics, University of St. Andrews, St. Andrews, Fife, KY16 9SS, U.K. e-mail: jamest@mcs.st-and.ac.uk; clare@mcs.st-and.ac.uk; ineke@mcs.st-and.ac.uk

² United Kingdom Atomic Energy Authority, Culham Science Centre, Abingdon, Oxfordshire, OX14 3DB, U.K. e-mail: k.g.mcclements@ccfe.ac.uk

³ Centre for Fusion, Space and Astrophysics, Department of Physics, University of Warwick, Coventry, CV4 7AL, U.K. e-mail: T.D.Arber@warwick.ac.uk

ABSTRACT

Context. This paper investigates the role of the Hall term in the propagation and dissipation of waves which interact with 2D magnetic X-points and considers the effect of the Hall term on the nature of the resulting reconnection.

Aims. The goal is to determine how the evolution of a nonlinear fast magnetoacoustic wave pulse, and the behaviour of the oscillatory reconnection which results from the interaction of the pulse with a line-tied 2D magnetic X-point, is affected by the Hall term in the generalised Ohm's law.

Methods. A Lagrangian remap shock-capturing code (Lare2d) is used to study the evolution of an initial fast magnetoacoustic wave annulus for a range of values of the ion skin depth (δ_i) in resistive Hall MHD. A magnetic null-point finding algorithm is also used to locate and track the evolution of the multiple null-points that are formed in the system.

Results. In general, the fast wave is coupled to a shear wave and, for finite δ_i , to whistler and ion cyclotron waves. Dispersive whistler effects cause rapid oscillations of the X-point, which (in combination with the arrival of the main body of the pulse) leads to the creation of magnetic islands and multiple null points under the influence of the Hall term. At later times, competition of local Lorentz and gas pressure forces return the system to a near-equilibrium state. The rate of oscillatory reconnection recovered during this latter phase appears to be unaffected by the value of δ_i .

Key words. Plasmas - Magnetohydrodynamics (MHD) - Waves - Magnetic reconnection - Sun: corona - Sun: flares

1. Introduction

The solar corona provides a rich dataset of magnetohydrodynamic (MHD) wave observations (see e.g. De Moortel 2005; Nakariakov & Verwichte 2005). Alfvénic and slow magnetoacoustic (MA) disturbances are generally constrained to propagate parallel to the local magnetic field, leaving any local magnetic structures unaffected by their passage. However, observations of fast MA waves (e.g. Aschwanden et al. 1999; Nakariakov et al. 1999; Wang & Solanki 2004; Ofman & Wang 2008) and globally propagating, large-scale disturbances (so called EIT waves, recently reviewed by Gallagher & Long 2011) show waves which may travel large distances, often across different magnetic field structures/environments. In doing so, they provide an opportunity to study the interaction and response of a range of magnetic environments and topologies with the incident wave(s). Of these wave-types, fast waves are often invoked in order to study magnetic reconnection, due to their ability to interact with coronal null-points; a general summary of

wave/null-point interaction studies can be found in McLaughlin et al. (2010).

Early studies of interactions between waves and magnetic null-points using MHD (e.g. Bulanov & Syrovatskii 1980) outlined how planar and perpendicular wave motions decouple and propagate independently, in the vicinity of 2D X-points. Various authors (e.g. Craig & Watson 1992; Hassam 1992; Craig & McClymont 1993; Ofman et al. 1993) have used a range of numerical and analytical techniques to expand on this initial premise, investigating the build-up and dissipation of current-sheets arising from the propagation of waves towards the null-point in cylindrical geometry. The presence of strong currents and non-ideal effects, such as resistivity and electron inertia, make it possible for magnetic reconnection to occur (in-depth summaries of the background and theory of magnetic reconnection may be found in Biskamp 2000; Priest & Forbes 2007; Birn & Priest 2007).

A recent series of papers by McLaughlin & Hood (2004, 2005, 2006) used linear MHD simulations to investigate various aspects of the behaviour of fast magnetoacoustic and shear

Alfvén waves in the vicinity of 2D magnetic X-points. They showed that, due to the decrease in Alfvén speed in the vicinity of the null, incident fast magnetoacoustic waves are refracted and accumulate at the null (while never actually reaching it, since $c_A \rightarrow 0$ as $B \rightarrow 0$). McClements et al. (2006); Ben Ayed et al. (2009) also discuss the coupling of shear and fast waves at X-points, in the respective limiting cases of weak and strong guide fields.

Of particular interest for this paper is the work of Craig & McClymont (1991). Using the linearised cold plasma resistive MHD equations, they found that the inertia of plasma flows, generated by an initial disturbance of an X-point from its equilibrium configuration, repeatedly carries the system past this equilibrium configuration, generating a series of oppositely oriented current sheets in a process known as oscillatory reconnection. More recently, McLaughlin et al. (2009) extended this work to include nonlinear and finite temperature effects.

The reconnection calculations described above are based on resistive MHD. If, as is generally assumed, the resistivity is due to electron-ion collisions, the low collisionality of the solar corona implies that significant energy release can only occur if the current density is extremely high and the magnetic field scale length is very small, thereby calling into question the self-consistency of the collisional model. Studies have suggested that a potential remedy to this problem might be to expand the traditional MHD description of plasma to also include additional effects from a generalised form of Ohm's law (for example, McClements et al. 2004, who included electron inertial effects in order to investigate the energy release mechanism associated with a solar flare). Numerical studies have suggested that models which include the Hall term in particular, may (in some circumstances) effectively return an enhanced rate of magnetic reconnection (see e.g. Birn et al. 2001; Birn & Priest 2007). Hall MHD models may therefore provide the simplest way to gain insight into the process of collisional reconnection. Analytical Hall MHD models of steady incompressible reconnection (Dorelli 2003; Craig & Watson 2005) have been used to investigate the conditions under which Hall currents can influence reconnection and Ohmic dissipation rates. More recently, Senanayake & Craig (2006) employ a numerical model to investigate the energy decay of a perturbed line-tied X-point system which also includes Hall effects. Craig & Litvinenko (2008) extended this model to obtain more detailed reconnection scalings, finding that the influence of Hall currents may be moderated by larger system sizes.

The goal of this work is to determine the extent to which 2D nonlinear wave/X-point interactions (as described by McLaughlin et al. 2009) are affected by the inclusion of the Hall term in Ohm's Law. To do this, we first outline the basic setup, equations and assumptions in Sect. 2. The initial behaviour of the nonlinear fast wave is described in Sect. 3, while the formation and evolution of the magnetic topology involving multiple null-points is explained in Sect. 4. The system ultimately set-

ties into an oscillatory reconnective regime, described in Sect. 5. A discussion of the nature of the reconnection is presented in Sect. 6, followed by a summary of conclusions in Sect. 7

2. Numerical model setup

The system was modelled numerically using a two dimensional version of a Lagrangian remap scheme (LareXd), described by Arber et al. (2001), which includes an optional Hall physics package to incorporate the Hall term into the standard MHD system of equations, seen here in normalised dimensionless form:

$$\begin{aligned}\frac{\partial \rho}{\partial t} + \nabla \cdot (\rho \mathbf{v}) &= 0, \\ \rho \left(\frac{\partial \mathbf{v}}{\partial t} + (\mathbf{v} \cdot \nabla) \mathbf{v} \right) &= (\nabla \times \mathbf{B}) \times \mathbf{B} - \nabla p, \\ \frac{\partial \mathbf{B}}{\partial t} &= \nabla \times (\mathbf{v} \times \mathbf{B}) - \nabla \times (\eta \nabla \times \mathbf{B}) - \lambda_i \nabla \times \left[\frac{1}{\rho} (\nabla \times \mathbf{B}) \times \mathbf{B} \right], \\ \rho \left(\frac{\partial \epsilon}{\partial t} + (\mathbf{v} \cdot \nabla) \epsilon \right) &= -p \nabla \cdot \mathbf{v} + \eta j^2,\end{aligned}$$

for dimensionless mass density ρ , pressure p , magnetic field strength \mathbf{B} , fluid velocity \mathbf{v} , internal energy density ϵ , resistivity η (the reciprocal of the Lundquist number) and ion skin depth λ_i . These equations have been normalised with respect to typical values of magnetic field strength (B_0), temperature (T_0) and number density (n_0). The velocities are scaled with the global Alfvén speed c_A ($= B_0 / \sqrt{\mu_0 m_p n_0}$, with proton mass m_p and permeability of free space μ_0), and time t_0 is scaled by the global Alfvén time, $t_0 = l_0 / c_A$, for a typical system lengthscale l_0 .

For example, adopting typical flaring coronal normalisation values of $B_0 = 100\text{G}$ and $n_0 = 10^{16}\text{ m}^{-3}$ implies velocities are normalised by $v_0 = c_A \approx 2\text{ Mms}^{-1}$. Adopting a typical flaring coronal temperature, $T_0 = 2 \times 10^6\text{ K}$, means that $\beta_0 \approx 0.007$ (where β_0 is the local plasma beta, $2\mu_0 p_0 / B_0^2$, defined at a radius l_0 from the origin). The role of the Hall term is quantified by the ion skin depth, δ_i . The normalised dimensionless ion skin depth used in the numerical scheme (λ_i) is given by:

$$\lambda_i = \frac{\delta_i}{l_0} = \frac{c}{l_0 \omega_{pi}},$$

with the ion plasma frequency ω_{pi} ($= \sqrt{n_0 e^2 / m_p \epsilon_0}$ for electron charge e and permittivity of free space ϵ_0) fixed through the number density n_0 . A choice of $\lambda_i = 0.0072$ implies a normalising lengthscale $l_0 \approx 0.3\text{ km}$, while increasing λ_i by a factor of 10 reduces l_0 by the same amount ($l_0 \approx 32\text{ m}$). Finally, the dimensionless plasma resistivity is determined using

$$\eta = \frac{\eta_0}{\mu_0 l_0 v_0},$$

where η_0 is the electrical resistivity ($= 1/\sigma$ for electrical conductivity σ). As pointed out by Craig & Litvinenko (2002), the levels of resistivity in the flaring corona may be as much as a factor of 10^6 higher than the collisional value. Using this enhancement factor and the normalisation described above, we find $\eta = 0.0005$ where $\lambda_i = 0.0072$, while a smaller enhancement (10^5) is produced with an identical level of η when $\lambda_i = 0.072$.

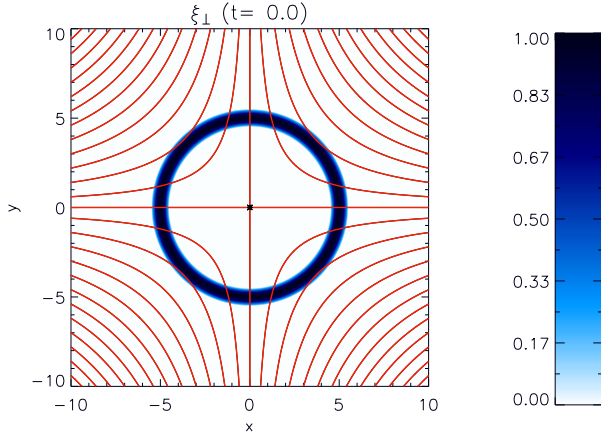


Fig. 1: Initial fast wave annulus amplitude, defined using ξ_{\perp} , centred on $r = 5$ with amplitude $A = 1$. Also overplotted are selected contours of A_z (seen in red), indicating the equilibrium field configuration $\mathbf{B} = [-x, y, 0]$ with the X-point location indicated in white (found using null-tracking routine of Haynes & Parnell 2007).

2.1. Equilibrium and initial conditions

A wide range of equilibrium magnetic field configurations have been studied in investigations of wave/null-point interactions (see McLaughlin et al. 2010, for a detailed review). In this investigation, our equilibrium is chosen to be

$$\mathbf{B} = [B_x, B_y, B_z] = [-x, y, 0]. \quad (1)$$

Note that this equilibrium configuration is curl-free (i.e. $\mathbf{J} = 0$ initially) and contains a single null-point, located at the origin. A common tool for providing visual representation of 2D magnetic fields is the magnetic vector potential \mathbf{A} , which (for the initial field configuration detailed in Eq. 1) is given by

$$\mathbf{A} = [0, 0, A_z] = [0, 0, C - xy],$$

where C is an arbitrary constant. Lines of constant magnetic flux can be illustrated using contours of A_z , as seen in Fig. 1, however this figure illustrates only selected contours of A_z over half of the simulated domain, $(x, y) \in [-10, 10]$.

A 5120×5120 grid was used to simulate a range $(x, y) \in [-20, 20]$. Reflective (zero gradient) boundary conditions were applied to all variables ($\mathbf{B}, \rho, \epsilon$) except velocities, which were fixed to zero at all boundaries. To aid direct comparison with McLaughlin et al. (2009), we retain their selection of natural system variables,

$$\xi_{\perp}(x, y, t) = (\mathbf{v} \times \mathbf{B}) \cdot \hat{\mathbf{z}} = v_x B_y - v_y B_x,$$

$$\xi_{\parallel}(x, y, t) = (\mathbf{v} \cdot \mathbf{B}) = v_x B_x + v_y B_y,$$

in order to specify our initial conditions:

$$\xi_{\perp}(x, y, 0) = A \sin[\pi(r - 4.5)] \quad 4.5 \leq r \leq 5.5,$$

$$\xi_{\parallel}(x, y, 0) = 0,$$

where $r = \sqrt{x^2 + y^2}$ (and also noting that velocities perpendicular and parallel to the local magnetic field may be found by scaling ξ_{\perp} and ξ_{\parallel} , i.e. $v_{\perp} = \xi_{\perp}/|\mathbf{B}|$ and $v_{\parallel} = \xi_{\parallel}/|\mathbf{B}|$ respectively). A visual representation of these initial conditions can also be seen in Fig. 1.

In anticipation of the annulus splitting into two wave pulses (which travel radially inwards and outwards) and in order to focus only on the part of the pulse which interacts with the null, all system variables outside a radius $r = 6$ were reset to their equilibrium values. This was performed at $t = 0.7\tau_A$, the point at which the waves were deemed to be sufficiently independent from one another that the outer pulse may be removed without affecting the inner pulse. At this point, a damping layer was also introduced for $r \geq 6$, removing kinetic energy from any waves which travel outwards beyond this radius, to avoid complications from reflection at the simulation boundaries.

3. Fast wave annulus evolution in Hall MHD

As mentioned above, the initial fast wave annulus (shown in blue in Fig. 1) splits into two oppositely travelling wave pulses, travelling radially inwards and outwards, with each pulse initially having amplitude $0.5A$. Using the MHD case (described in McLaughlin et al. 2009) as a benchmark, the effect of the Hall term on the splitting of the wave pulse is illustrated in the first column of Fig. 2, for both the $\lambda_i = 0.0072$ and $\lambda_i = 0.072$ simulations.

In particular, the behaviour of the pulse in the $\lambda_i = 0.0072$ regime demonstrates many similarities with the equivalent MHD case; the inner pulse retains its initial profile, and is subject to refraction as it approaches the null point across the magnetic field lines. With no initial parallel velocity ($\xi_{\parallel} = 0$) and our choice of equilibrium field (Eq. 1), the system naturally develops an asymmetry in wave-speed (due to the creation of a “background inflow” in the upper-left and bottom-right quadrants, while a “background outflow” is seen in the upper-right and bottom-left quadrants; see Fig. 4 of McLaughlin et al. 2009, where vertical and horizontal asymmetries are obtained due to the same effect). Thus, the initial velocity profile causes the peak of the pulse to propagate faster than the edges in the upper-left and lower-right quadrants, while the pulse edges travel faster than the peak in the upper-right and lower-left quadrants. These wave-speed asymmetries become discontinuous, and lead to the formation of fast-oblique (and perpendicular) shocks, as identified by McLaughlin et al. (2009). These shock fronts are associated with abrupt changes in density and temperature which coincide with discontinuities in the magnetic field, as seen in Fig. 3.

In Hall MHD, differences begin to arise in comparison to the MHD benchmark, which increase in proportion to the value of λ_i . Threlfall et al. (2011) demonstrated that the inclusion of the Hall term in the generalised Ohm’s law causes an initially shear Alfvén wave pulse (acting along a uniform magnetic field) to decouple into whistler and ion-cyclotron wave components, each

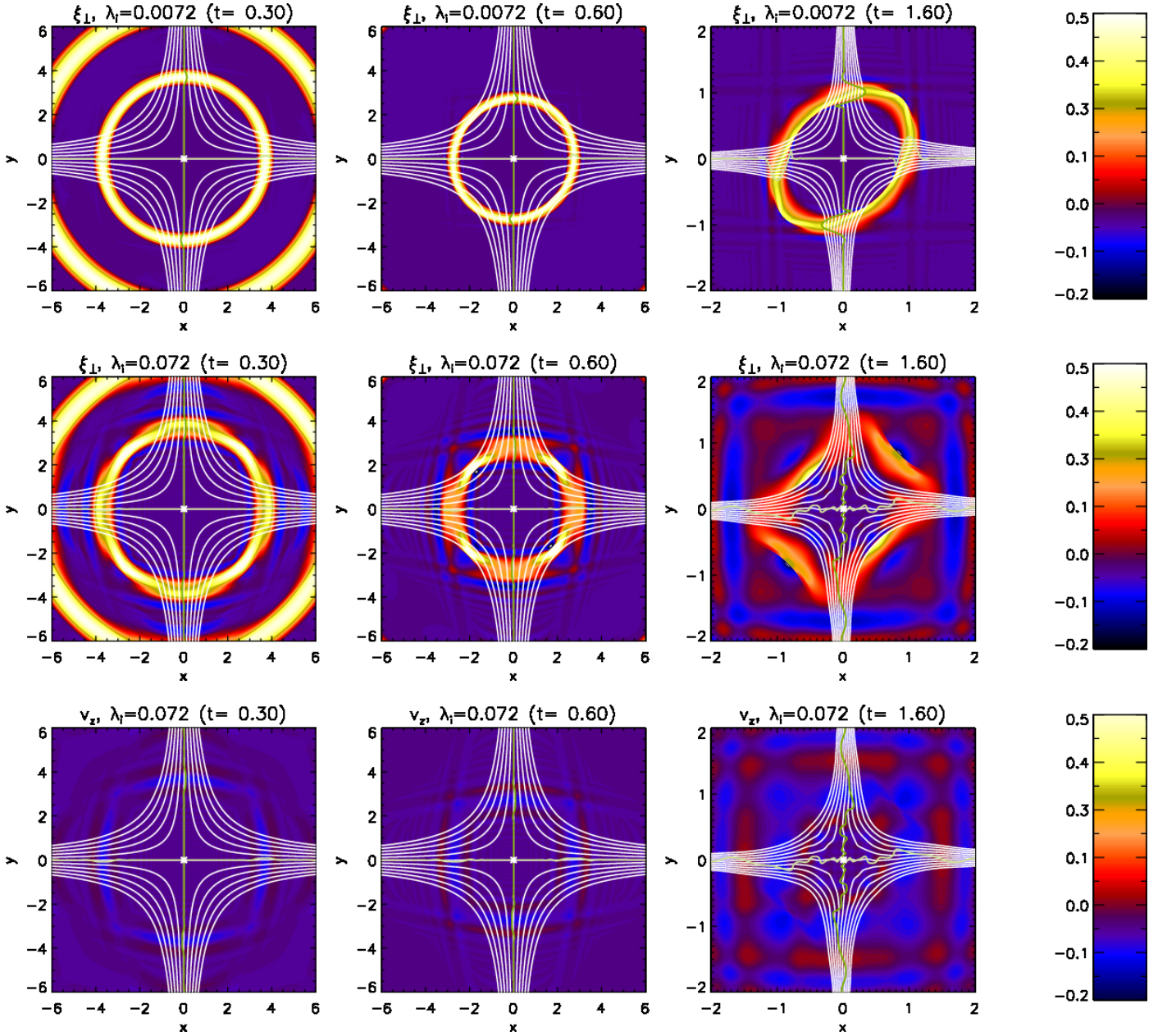


Fig. 2: Contours of ξ_{\perp} (top and middle) and v_z (bottom) seen through snapshots in time, for $\lambda_i = 0.0072$ (top), and $\lambda_i = 0.072$ (middle and bottom). Each case is overplotted with selected flux surfaces (contours of A_z - in white), the lines of $B_x = 0$ (dark green) and $B_y = 0$ (light green), and also the location of the null-point (indicated by a white star). (NB. while the first two columns display $(x, y) \in [-6, 6]$, the final column zooms in to illustrate a range of only $(x, y) \in [-2, 2]$ of the entire simulated range, $(x, y) \in [-20, 20]$).

having opposite circular polarisation. In this experiment, we see that the initially fast-mode wave pulse also becomes decoupled in this way, due to the inclusion of the Hall term. While much of the behaviour seen in the $\lambda_i = 0.0072$ simulations matches that seen in the MHD benchmark case, the second and third rows of Fig. 2 show that increasing the effect of the Hall term also increases the amount of coupling to the shear velocity component, v_z . The asymmetry of wave-speed (described earlier) is also retained in simulations with $\lambda_i = 0.072$, however the coupling to other wave modes and enhanced dispersion (which ac-

company the Hall term) limit the formation of the fast-oblique parts of the shock front. The second row of Fig. 2 illustrates this, showing that the shock front begins to take on the shape of the local magnetic field in this limit. The remaining wave annulus is concentrated at the centre of the four quadrants (where it remains exactly perpendicular to the local magnetic field, i.e. only the perpendicular shock fronts remain). Figure 3 shows that cuts through these shock fronts now reveal much larger density and temperature changes than in the $\lambda_i = 0.0072$ (and MHD benchmark) case(s).

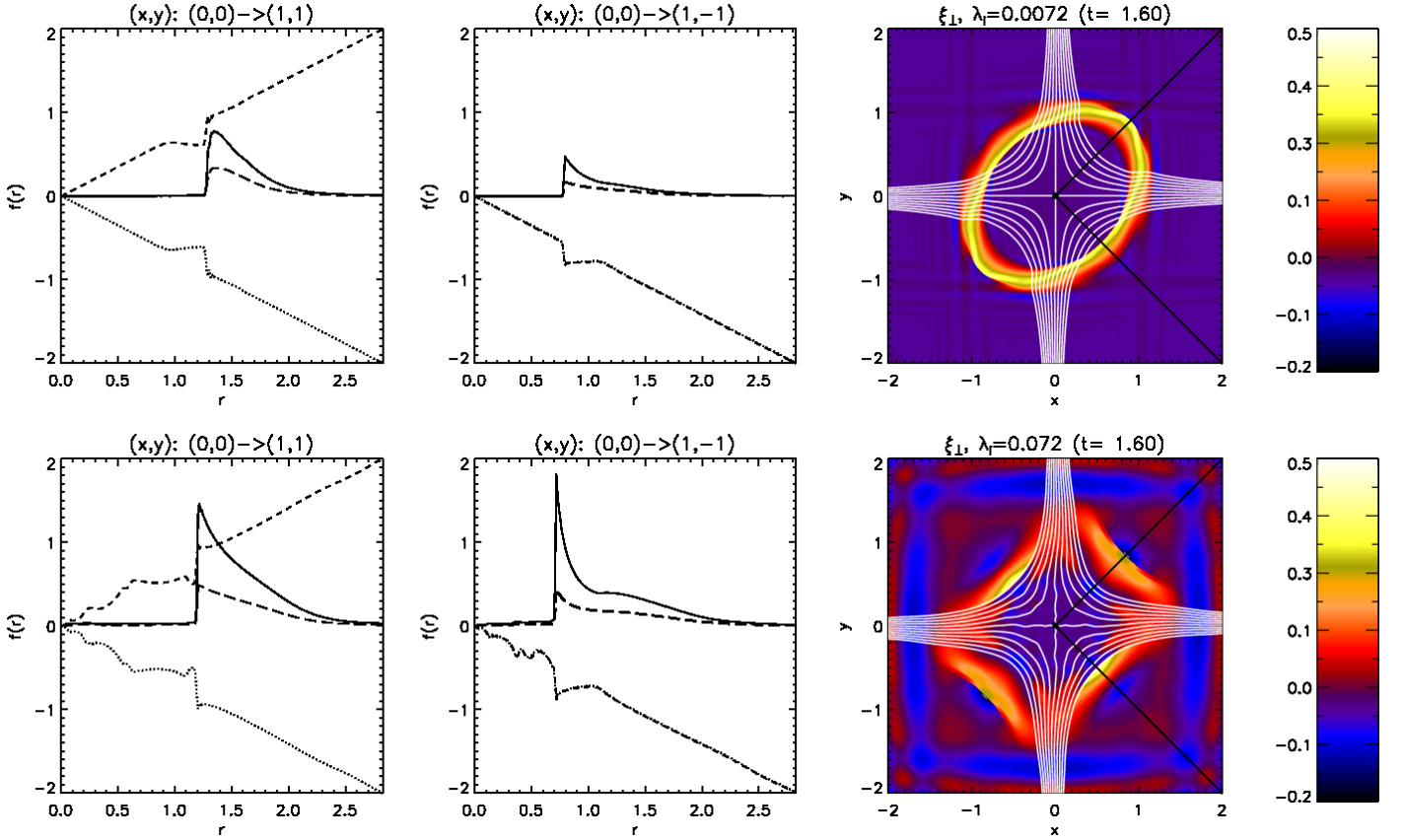


Fig. 3: Plots illustrating the jump conditions across the shocks in the system at $t = 1.6\tau_A$ for different ion skin-depth values. Cuts through the shock wave front illustrate radial variations in B_x (dotted line), B_y (short dashes), gas pressure p (solid line) and temperature T (long dashes) for a radius $r = \sqrt{x^2 + y^2} \in [0, 2\sqrt{2}]$ (p and T are enhanced by a factor of 50 to aid visual comparison). The positions of the cuts are indicated in the third column by the diagonal black lines, seen together with background contours of ξ_\perp and selected contours of A_z (in white).

Note that the diffraction-like pattern recovered in Figs. 2 and 3 are not related to any contact with a boundary, as these figures represent only a small region of the entire simulated domain, $(x, y) \in [-20, 20]$.

4. X-point collapse and evolution of magnetic topology

The response of the magnetic field to the inward-travelling pulse and the evolution and formation of current sheets greatly depends on the normalised ion-skin depth, λ_i . In the case where $\lambda_i = 0.0072$ (as with the MHD benchmark) the evolution of the system largely follows that outlined by McLaughlin et al. (2009); fast magnetic shock waves, formed in opposite quadrants, travel in towards the null, significantly deforming the magnetic field-lines as they pass. The initial interaction between the wave annulus and the null may be seen in Fig. 4.

In this limit (and in MHD), the outer edges of the shock front begin to overlap at $t \sim 2\tau_A$ [at approximately $(x, y) = (1, 1)$ and $(x, y) = (-1, -1)$], leading to the formation of hot “cusp” jets which heat the plasma (in the opposite quadrants to those where the original fast shocks predominantly formed). The centre of the

fast shock-fronts reach the null and begin to pass through each other at $t \approx 2.9\tau_A$, whereupon the local magnetic topology has deformed into a thin current sheet-like structure. The fact that the wave is able to reach and pass through the null is entirely due to our choice of a large initial wave amplitude and the nonlinear effects which result; a small amplitude wave would slow while approaching the null but never actually reach it (as $c_A \rightarrow 0$).

After $t \approx 2.9\tau_A$, the original fast shock-waves begin to pass through the null, allowing wave energy to travel out from the centre. This energy is removed from the system before any waves reach the simulation boundaries, due to the presence of the damping layer. Meanwhile the hot cusp-jets continue to grow and spread out, leading to the formation of further magnetic shocks which, in combination with a local increase in gas pressure, act to compress the initial current sheet and wedge open the separatrices. This ultimately causes the magnetic field to overshoot its equilibrium configuration, leading to the formation of a second current sheet, of opposite orientation in J_z and perpendicular to the original current sheet (i.e. from top-left to bottom right). The system then relaxes through a series of these current sheets, a process which is described in detail in Sect. 5.

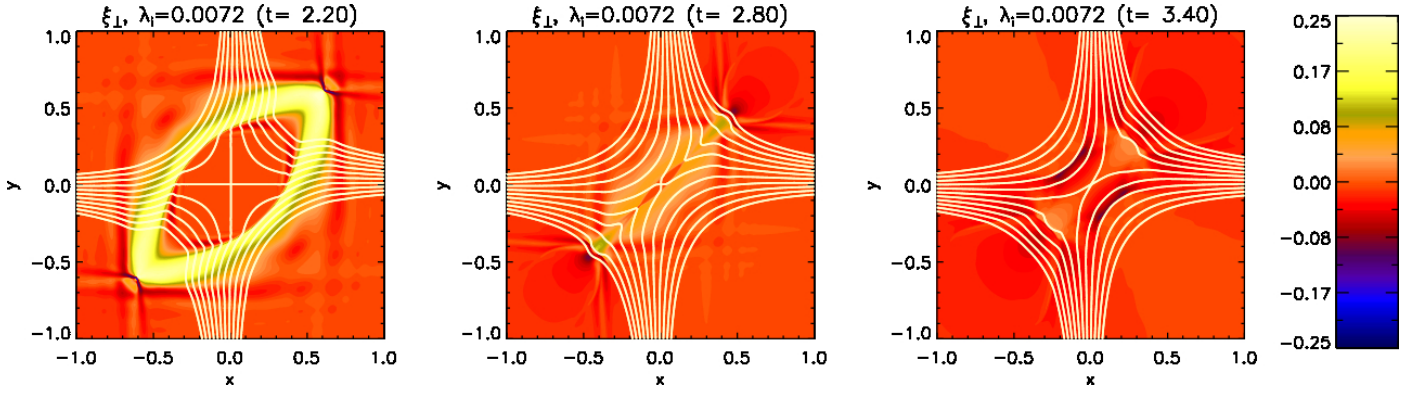


Fig. 4: Illustration of pulse evolution and X-point collapse in simulations where $\lambda_i = 0.0072$, following the formation of magnetic shocks; contours of ξ_\perp are seen at various times and overlaid with selected contours of A_z (in white).

Increasing λ_i by a factor of 10 highlights several marked differences with evolution outlined above, both in the way in which the wave annulus interacts with the local field and the field response. As mentioned earlier, the fast wave is not only coupled to a shear component of velocity through the inclusion of the Hall term, but also now contains both whistler and ion-cyclotron waves. In particular, dispersive whistler waves allow information to travel faster than both the local Alfvén and fast MA wave speeds. In the $\lambda_i = 0.072$ simulations, whistler waves are responsible for rapid oscillations of the magnetic field near the origin, at a much earlier time than the $\lambda_i = 0.0072$ results (and also in MHD); these early oscillations are demonstrated in the contours of $B_x = 0$ and $B_y = 0$ in the third column of Fig. 2. As the oscillations grow in amplitude, multiple additional nulls are created in a small region close to the origin (of radius $r \sim 0.5$). The additional nulls appear in pairs (containing both an X-type and O-type null); each new null pair is evidence of local magnetic reconnection. Every null point is located to sub-grid resolution accuracy using a linear interpolation algorithm (described in detail in Haynes & Parnell 2007), with the results catalogued in Table 1 according to phases during the simulations which display similar properties (such as number of nulls, local current sheet orientation, etc.). As we are using interpolation, the precise location of the nulls must be regarded as an approximation (with the error on the order of a fraction of the grid resolution).

Many of the early phases containing multiple nulls (phases 2-4 of Table 1) are highly dynamic; the number and position of nulls varies rapidly, and phases (with the same number of nulls) are relatively short-lived. All null points which arise as a result of the dispersive whistler component exist only on or close to the lines $y = x$ or $y = -x$, while any current sheets which form in the system also evolve rapidly and are short-lived. The formation of the whistler-generated nulls may be seen in the first row of Fig. 5, with subsequent rows illustrating the later evolution of nulls and currents in the system.

It is interesting to note that the behaviour of the MHD/ $\lambda_i = 0.0072$ simulations is encapsulated by only 3 of the phases outlined in Table 1. In these cases, the initial configuration

Table 1: Configuration of Nulls

| Phase | Nulls (X+O) | X's | O's | Central Null | Time | C-S Orientation |
|-------|----------------|-----|-----|-----------------|-----------|--------------------|
| 1 | 1 | 1 | 0 | X | <2.3 | n/a |
| 2 | 5 | 3 | 2 | X | 2.3 | / |
| 3 | 7 | 4 | 3 | O | 2.4 | \ |
| 4 | 5 | 3 | 2 | X | 2.5 | \ |
| 5a | 5 | 3 | 2 | X | 2.60 | \ |
| 5b | 1 | 1 | 0 | X | 2.61-2.64 | \ |
| 5c | 1 | 1 | 0 | X | 2.65-2.66 | / |
| 5d | 3 | 2 | 1 | X [†] | 2.67 | / |
| 5e | 5 | 3 | 2 | X | 2.68 | / |
| 6 | 3 | 2 | 1 | O | 2.69-3.4 | / |
| 7 | 7 | 4 | 3 | O | 3.5-3.6 | / |
| 8 | 5 | 3 | 2 | O [†] | 3.7 | / |
| 9 | 7 | 4 | 3 | O | 3.8 | / |
| 10 | 3 | 2 | 1 | O | 3.9-4.5 | / |
| 11 | 1 | 1 | 0 | X | >4.6 | * |

Notes. Summary of the configuration of null-points in the $\lambda_i = 0.072$ simulations, broken down into phases which display similar properties. In each phase, the number of nulls in the system and their type are given, along with the central null type, the time over which the phase occurs and the orientation of any local current sheets (/ infers a current sheet oriented along the line $y = x$, and \ along the line $y = -x$). [NB. [†] denotes a null asymmetry - the “central null” refers to the null closest to the origin in these instances; * denotes that the current sheet orientation alternates periodically via oscillatory reconnection].

(phase 1) is retained until the arrival of the fast-shocks at the null (phase 5c), after which the system relaxes through the oscillatory reconnection phase (11). The additional phases which occur only in the $\lambda_i = 0.072$ case are generated by the whistler components (for phases 2-5c), and following the arrival of the pulse, by a combination of whistler and ion cyclotron (fast and shear) wave components (phases 5d-10).

Using Table 1 and Fig. 5, the remaining evolution of the $\lambda_i = 0.072$ system may be described as follows; the arrival of two perpendicular magnetic shocks at the origin (originating from the upper-left and lower-right quadrants) halts the rapid os-

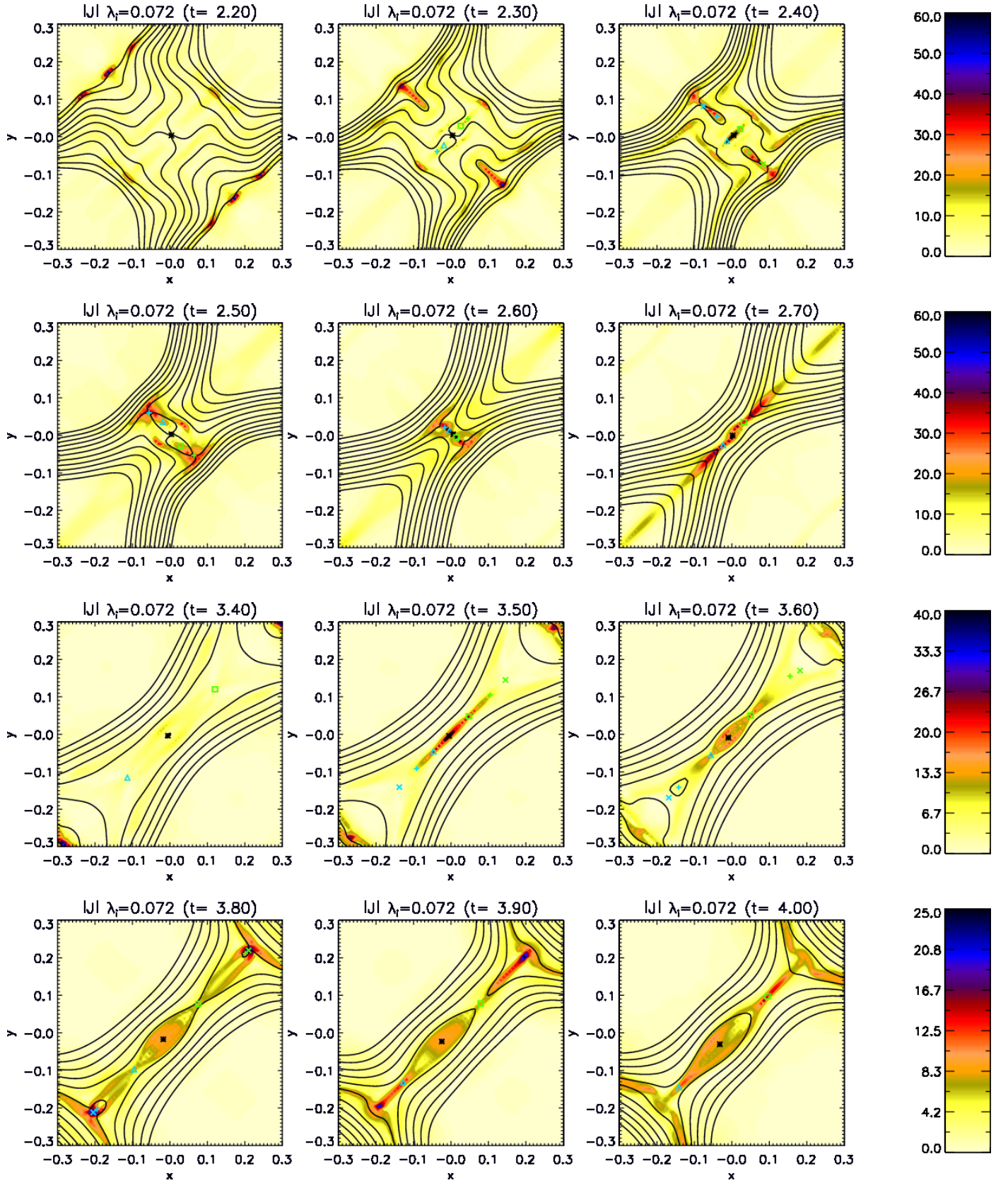


Fig. 5: Contours of current, $|J|$, illustrating snapshots of the $\lambda_i = 0.072$ simulations, focussing closely on behaviour near the null, highlighting the presence and locations of multiple nulls, overlaid with selected contours of A_z (in black). Each null is assigned a symbol and a colour based on the null position relative to the central null, which is indicated by a black star. Nulls above this along the contour of $B_y = 0$ would be seen in green and those below are shown in light blue. The distance along the $B_y = 0$ line is indicated by the symbol - a snapshot containing 7 nulls would thus display, from left to right, $\times + \triangle * \square + \times$.

cillation of the field in the local vicinity. This is illustrated in phase 5b of Table 1, highlighting that the shock fronts cause all additional null pairs to recombine, leaving a single X-type null at the origin. The arrival of these shock fronts at the remaining null, between $2.64\tau_A < t < 2.65\tau_A$, reverses the orientation of the currents generated by earlier whistler oscillations (seen in the second row of Fig. 5). The remaining shock waves then continue to pass through the origin and each other, forming a relatively stable current sheet oriented along the line $y = x$ (as with the previous MHD/ $\lambda_i = 0.0072$ simulations). Unlike the previous cases, multiple null pairs are then created, at a range of locations which all lie along the current sheet, up to a maximum of 6 additional nulls at any one time. At $t \approx 2.69\tau_A$ (phase 6 of Table 1), the appearance of a null pair close to the origin causes the existing X-type null to be displaced from the origin, with a new O-type null-point taking its place at the centre. The central null remains as O-type until $t \approx 4.5\tau_A$. Islands of current form around the O-type nulls in the system, and, in particular, at this long-lived central O-type null (demonstrated by the final row of Fig. 5).

Phase 11 of Table 1 marks destruction of the additional null pairs, leaving a single X-type null at the origin. This coincides with the arrival of the second (slower) pair of shock waves from the upper-right and lower-left quadrants (the formation of which may be seen in the second rows of Figs. 2 and 3). These shocks arrive much later than the initial shocks which cause the initial X-point collapse (due to the wave-speed asymmetry discussed earlier), and cause any remaining additional nulls to merge. At this point the system returns to the original configuration; a single X-type null-point at the origin about which forms a series of oppositely oriented current sheets, as with previous MHD/ $\lambda_i = 0.0072$ cases.

5. Oscillatory relaxation

Both in the MHD and Hall MHD simulations, the majority of the initial transient wave features have left the system by $t \approx 10\tau_A$, and no longer disturb the null. At this point, the perturbed field begins to evolve back to a force-balanced state through a series of oppositely oriented current sheets, reconnecting magnetic flux at the single X-type null-point as it relaxes (see e.g. Craig & McClymont 1991; McLaughlin et al. 2009).

In the MHD/ $\lambda_i = 0.0072$ investigations, only a single null is ever present, located at the origin, where no initial current density is recorded prior to the arrival of the fast wave (at approximately $\sim 2.9\tau_A$). Threlfall et al. (2011) showed that the dispersion relation derived for the long wavelength Hall MHD regime yields a modified form of the MHD dispersion relation. In this limit, the whistler and Alfvén speeds are well matched, but moving to the short wavelength Hall MHD limit rapidly increases the whistler speed in comparison to the Alfvén speed. Thus the MHD/ $\lambda_i = 0.0072$ simulations begin to destabilise the magnetic field at the origin at approximately the same time (as

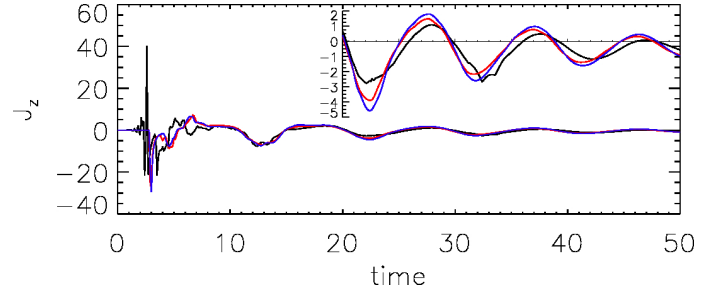


Fig. 6: Comparison of the time evolution of the out-of-plane current, J_z , at the central null. The black line indicates the value of J_z for the central null in the $\lambda_i = 0.072$ simulations, overlaid with the $\lambda_i = 0.0072$ results (in red) and the MHD results (in blue). The insert displays the behaviour of all 3 cases at later times but over a much smaller range of J_z in the y-axis).

seen in Fig. 6) but this destabilisation occurs much earlier in simulations with $\lambda_i = 0.072$.

The arrival of the fast-wave at the null (seen in Fig. 4 for the case where $\lambda_i = 0.0072$) forms a strong current sheet at the origin. This is seen as the deep initial minima in the blue and red curves of Fig. 6. This current sheet is then destabilised both by the remaining fast-wave exiting the system, and the “wedging open” of the magnetic field by the cusp jets described earlier (and studied in detail by McLaughlin et al. 2009). The preferred direction for the generation of a current sheet (noted by McLaughlin et al. 2009) results from the orientation of the initial current sheet (formed by the arrival of the fast shocks). This orientation also determines in which quadrants plasma pressure is increased; the fast/perpendicular shocks compress and heat plasma, particularly to the left and right of the current sheet. The plasma pressure enhancement which results then exerts a force to open the compressed X-point quadrants, and return the system to equilibrium. The first peak of the MHD/ $\lambda_i = 0.0072$ curves in Fig. 6 signals the formation of a second current sheet, of opposite orientation, generated by the field overshooting its initial equilibrium configuration. While minor cusp jets are also observed during this phase (once again causing the magnetic field to widen), they are seen to be much weaker and are not observed in any further oscillation cycles; hence they do not play an essential role in the subsequent oscillatory process.

The oscillatory nature of the experiment (at stages where the cusp jets are no longer seen) is generated by a competition of Lorentz and gas pressure forces, each in turn restoring an overshoot of the equilibrium configuration brought on by the other. A simplified description of this competition of forces may be seen in Fig. 7. Of the Lorentz force components, magnetic pressure dominates in these experiments (magnetic tension aids the compression of magnetic field lines in the compressed quadrants of the X-point as the current sheet forms). As each successive overshoot is smaller than the last, the system is ultimately able to relax.

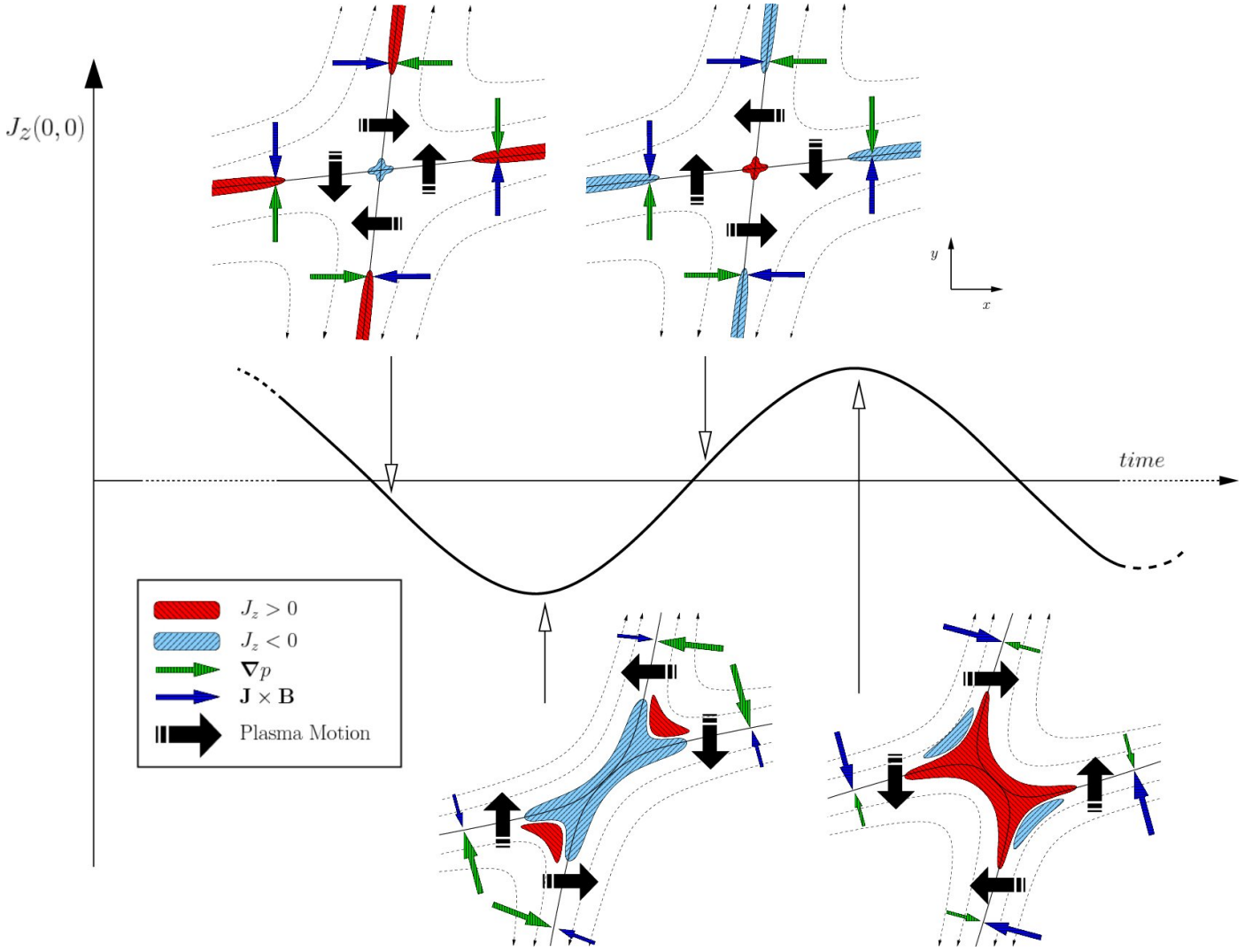


Fig. 7: Cartoon illustrating the cycle of forces generated during the oscillatory reconnection phase (for key to symbols, see legend).

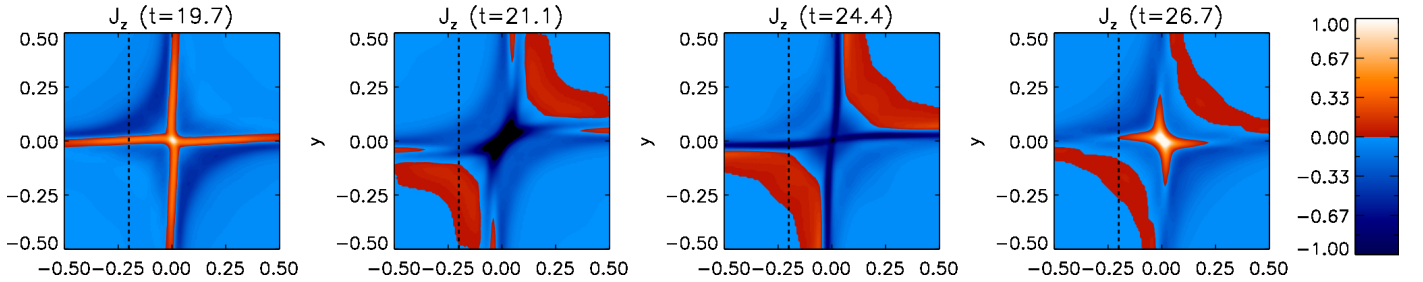


Fig. 8: Illustration of current sheets generated during oscillatory phase. Each snapshot displays normalised perpendicular current, J_z , in a region near the X-point, $x, y \in [-0.5, 0.5]$, at selected times during the oscillatory cycle (chosen for comparison with Fig. 9, which displays quantities along a cut indicated in each frame by a dashed black line).

We also present supporting evidence for this competition of forces, in the form of snapshots of the local current configuration near the null (Fig. 8) and a summary of the forces and velocity flow in a cut through one of the separatrices (Figs. 9a and 9b respectively), sampled at the same time. Beginning at $t = 19.7\tau_A$, the chosen cycle begins with Lorentz and gas pressure forces approximately balanced and a strongly negative plasma veloc-

ity (Fig. 9 - solid lines), while Fig. 8 shows that the plasma is close to its original configuration (and that a previous strong positive J_z current sheet at the origin is diminishing as the field returns towards equilibrium). A large plasma velocity (acting downward along the chosen cut) generates inertia, which drags field lines past their equilibrium configuration, compressing the plasma in the lower-left and upper-right quadrants. Subsequently

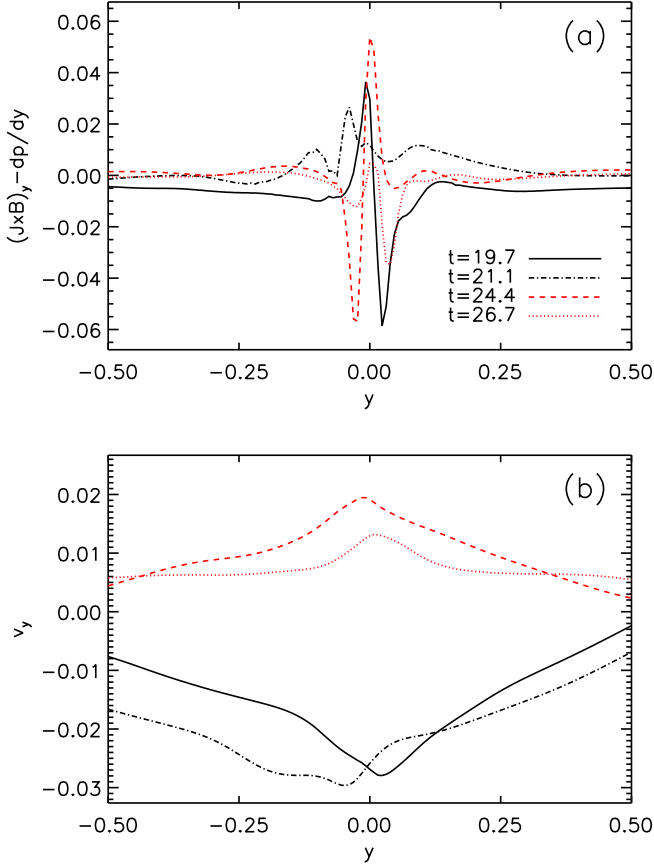


Fig. 9: y -components of (a) a summation of Lorentz and gas pressure forces and (b) velocity in a cut along the y -axis at selected times; the timing of each cut is chosen for comparison with the local current configurations demonstrated in Fig. 8 (where the location of each cut is also illustrated by a dashed black line). One half of the oscillatory cycle is indicated in red, with the remaining half in black (at times indicated in the legend).

a gas pressure response is generated in these quadrants. Along the cut, a strong gas pressure force acting upwards dominates the competition of forces at $t = 21.1\tau_A$ in Fig. 9a (dot-dashed lines). Concurrently, a current sheet (of negative J_z and of opposite orientation to the first) has formed in the corresponding panel of Fig. 8. The force imbalance slows the plasma; in Fig. 9b, the plasma velocity reaches its largest negative value and reverses sign as it accelerates back towards an equilibrium state. Having once more returned to a near-equilibrium field configuration (at $t = 24.4\tau_A$), Fig. 9a (dashed lines) shows Lorentz and gas pressure forces are near-balanced, but the large upward velocity in 9b now carries plasma past equilibrium in the opposite direction (compressing the upper-left and lower-right quadrants). Note that the velocity seen here is approximately at maximum for this particular phase of the cycle, but is much smaller than the equivalent maximum downward velocity generated earlier; each successive peak is smaller than the last as each overshoot grad-

ually reduces in size as the system relaxes. In the final snapshot (at $t = 26.7\tau_A$), Fig. 8 shows the formation of a positive J_z current sheet near the origin, while the plasma velocity has begun to reduce (Fig. 9b, dotted lines). The reduction in plasma velocity is caused by a second force imbalance (where forces along the cut are now dominated by contributions from the Lorentz force, acting downward in 9a). Plasma velocity continues to reduce and the forces return to balance once more; with the plasma returning towards its equilibrium configuration the cycle repeats.

6. Nature of reconnection

The reconnection which takes place in our system may be broadly grouped into two categories, associated with either the initial X-point collapse or the later oscillatory relaxation. While the oscillatory reconnection process is very similar in all 3 experiments, the initial X-point collapse differs greatly as the influence of the Hall term increases.

For the $\lambda_i = 0.0072/\text{MHD}$ benchmark simulations, the wave annulus reaches the null at approximately $t \sim 2.8\tau_A$, causing the initial departure from zero of J_z at the null, plotted in Fig. 6 (red and blue lines), and thus marking the onset of reconnection. Following this, the reconnection associated with the initial X-point collapse follows the description given in McLaughlin et al. (2009). The initial current sheet (aligned with the line $y = x$) is “wedged open” by the formation of cusp jets, forming a second current sheet perpendicular to the first. This second current sheet (aligned with the line $y = -x$) is maintained until the oscillatory reconnection phase (discussed earlier and below) starts at around $t \sim 10\tau_A$. In simulations with $\lambda_i = 0.072$, the onset of reconnection occurs much earlier, when a rapid oscillation of the field at the origin (due to the whistler wave component) creates multiple X-type and O-type null-points, which by their very existence provide evidence of local magnetic reconnection. In Fig. 10a, we show how the number of nulls and the local current at each null varies in both Hall MHD experiments. The arrival of perpendicular magnetic shocks causes the multiple nulls to recombine, leaving a single X-type null about which a single large current sheet forms. Subsequently, further nulls are generated within this current sheet, which is ultimately collapsed by a second pair of shocks; these shocks cause the nulls to recombine once more, after which only a single null remains at the centre, with the oscillatory phase once more setting in at around $t \sim 10\tau_A$.

During the initial X-point collapse phase, large currents (both perpendicular and planar) are often associated with many of the nulls in the system (regardless of type) as indicated by Figs. 10b and 10c. These currents provide insight into the local reconnection rate at each null. It is clear from 10b and 10c that the currents at the nulls during the $\lambda_i = 0.072$ case are typically larger than those during the $\lambda_i = 0.0072/\text{MHD}$ cases, indicating that the rate of reconnection increases with the value of λ_i , as one might expect.

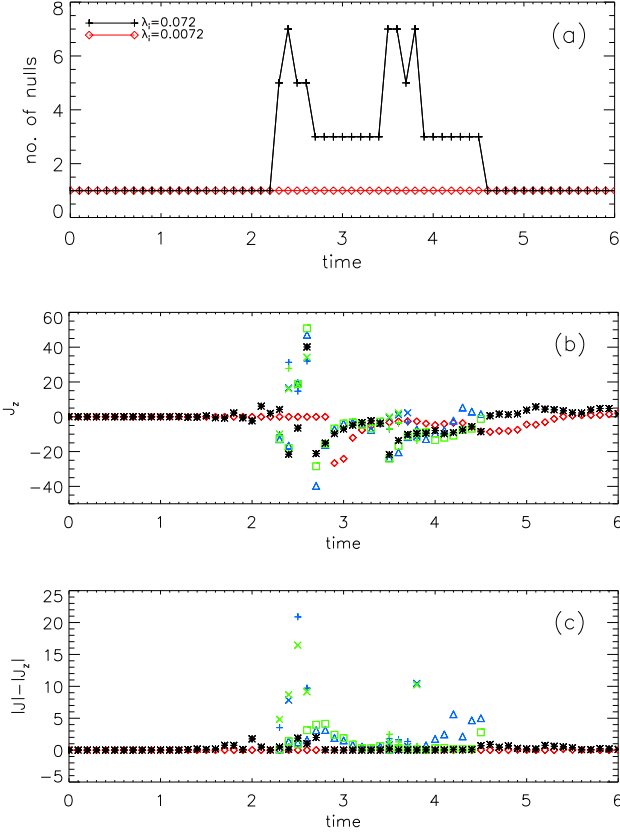


Fig. 10: Figure (a) indicates the number of nulls present in the Hall MHD simulations. The remaining figures illustrate the evolution of current at each null; the values of (b) J_z and (c) $|\mathbf{J}| - |J_z|$ at an individual null are shown, comparing the single null case ($\lambda_i = 0.0072$, in red) with values at every null in the $\lambda_i = 0.072$ simulations. When multiple nulls are present, each null is uniquely identified by a combination of colour and symbol, identical to that outlined in Fig. 5 [e.g. 7 nulls, ordered according to location along the $B_y = 0$ line, would be identified by $\times + \triangle * \square + \times$].

How each local rate contributes to a global rate (for a system containing multiple X-type and O-type nulls which continually change in number and position) is unknown. In 2D, reconnection can only occur at X-points, while annihilation/dissipation and generation of magnetic flux is associated only with O-points (pp. 41, [Birn & Priest 2007](#)). Annihilation and generation of magnetic flux are distinct from reconnection since they involve a loss or a gain of magnetic flux rather than a transfer of flux between topologically distinct regions. In the $\lambda_i = 0.072$ simulations, where there are multiple nulls, reconnected flux from one X-point may reconnect again at another X-point, repeating this process several times. It is still an open question as to whether repeated reconnection should or should not be taken into account when determining an overall (i.e. global) rate of reconnection. Additionally, flux pile-up may occur at O-points, which again may or may not affect a global reconnection rate.

Calculation of a global reconnection rate through a summation of rates at individual X-points (for example) would be insufficient to describe all the reconnection which takes place. The sign of the reconnection rate (seen through the orientation of the local electric field) at each X-point varies significantly (according to Fig. 10); nulls with similar rates which are opposed in sign would cancel if all rates were simply summed, obscuring the true amount of reconnection which has taken place. The variation of the position of each null also calls into question whether a single (global) diffusion region or several smaller diffusion regions are present in Hall MHD reconnective regimes. Finally, in some cases, a significant fraction of the total current at a null may be located in one or both of the planar components, J_x and J_y , as seen in Fig. 10c. How these currents affect reconnection in a 2D model requires further consideration.

The second category of reconnection, as already mentioned, is oscillatory and involves just a single null in all experiments considered. Despite the different skin depths in the experiments, both MHD and Hall MHD simulations yield nearly identical frequencies of current oscillation at the central null (albeit with a phase-difference in the $\lambda_i = 0.072$ case, as seen in Fig. 6).

[Craig & McClymont \(1991\)](#) studied the oscillatory relaxation of a 2D X-point field following a perturbation with well defined azimuthal modes. They obtained analytical solutions which included an expression for the oscillation period of the lowest frequency, associated with the most slowly decaying eigenfunction of their system which relaxes through oscillatory reconnection. This analytical treatment, when performed for a purely azimuthal (i.e. $m = 0$), fundamental radial mode ($n = 0$), yields a period of oscillation for topological reconnection, which depends only on the Lundquist number:

$$\tau_{\text{osc}}^{n=0} = 2 \ln S,$$

where $\tau_{\text{osc}}^{n=0}$ is in units of Alfvén times, $\tau_A = l_0/c_A$. Substituting the Lundquist number for our experiment ($S = 2000$) yields an oscillation period $\tau_{\text{osc}}^{n=0} \approx 15.2$, which is significantly higher than the period of oscillation seen from the oscillation of current at the null in Fig. 6, which we estimate to be $\tau_{\text{osc}} \approx 10$.

The smaller oscillation time in our simulations compared to the value given by the above equation may be explained by the fact that the latter applies only to the lowest frequency radial eigenmode of the system considered by [Craig & McClymont \(1991\)](#). In contrast, the fast wave modelled in our simulation contains many radial eigenmodes, with a range of frequencies higher than that of the fundamental mode. Furthermore we employ damping layers and a non-circular boundary that differs from that of the system considered by [Craig & McClymont](#). Finally, nonlinear effects in our simulations cause the annulus to become azimuthally asymmetric, introducing coupling to finite m modes, for which [Craig & McClymont](#) did not compute any eigenfunctions. It is therefore to be expected that while the overall oscillation period we obtain is of the same order as the fundamental mode period found by [Craig & McClymont](#), the presence of higher frequency radial eigenmodes, nonlinear effects and the

choice of boundary conditions means that the period in the simulation differs from that obtained by these authors.

7. Discussion and conclusions

Simulations of an X-type null point disturbed from equilibrium by an incident nonlinear fast wave annulus behave largely as described by McLaughlin et al. (2009), both in MHD and in Hall MHD simulations with a small ion skin depth value. Increasing the ion-skin depth by a factor of 10 shows significant differences, both in the evolution of the initial annulus and the response of the local magnetic environment. The initial fast wave annulus rapidly deforms, coupling to a shear component which may only travel along magnetic field lines. The oblique parts of the shock front seen in the MHD benchmark/ $\lambda_i = 0.0072$ cases are no longer present, leaving most of the remaining fast wave concentrated in four perpendicular shock fronts. The dispersive whistler waves cause the field near the null to rapidly oscillate, even before the arrival of the shock fronts. As the waves from different quadrants arrive out of phase with one another, multiple null pairs are generated near the equilibrium X-point location, prior to the arrival of a pair of perpendicular magnetic shocks at the null. The initial shocks set up a current sheet containing an island of current surrounding an O-type null at the centre, with up to 6 additional nulls at either side. A second slower pair of perpendicular shocks (arriving from the opposite quadrants to the first) destabilise the current sheet, causing all additional nulls to recombine, leaving a single X-type null remaining at the origin.

Following the initial X-point collapse, all simulations undergo oscillatory reconnection, through which the system is able to relax. Both in MHD and Hall MHD, plasma pressure is enhanced at both ends of the initial current sheet, which exerts a force to open the magnetic field lines in the compressed quadrants, in an attempt to restore equilibrium. As the field nears its original configuration, both the gas pressure and Lorentz forces balance each other, but plasma inertia causes the field to overshoot, forming a second (perpendicular) current sheet. A Lorentz force response accelerates plasma back towards its equilibrium configuration once more, and the cycle repeats; each additional overshoot is smaller than the last, and requires a smaller restoration force as the system returns to equilibrium.

While the appearance and recombination of additional null-points in the simulations where $\lambda_i = 0.072$ is evidence that magnetic reconnection is occurring, the presence of additional nulls makes it difficult to determine a global reconnection rate. The frequency of oscillation of the later relaxation phase is seen to closely match in the MHD and Hall MHD cases considered; this suggests that the rate of reconnection associated with oscillatory relaxation is independent of skin-depth.

Several extensions to this work merit further consideration. For example, introducing an initially non-zero plasma beta may significantly alter the balance of forces in the oscillatory cycle, potentially affecting the oscillation frequency and hence the

rate of reconnection during the oscillatory phase. This would also introduce slow magnetoacoustic waves into the problem; in Hall MHD, the additional presence of coupled fast and shear Alfvén wave motions would further complicate any identification of specific wave modes. Altering the form of the initial disturbance (even simply in MHD) would alter the wave-speed asymmetry and hence affect the arrival of the initial perpendicular shock-waves at the null. Finally, full 3D Hall MHD studies of separator/null-point reconnection (for example) would allow a more comprehensive comparison between the full vector forms of the magnetic vector potential, \mathbf{A} , and current \mathbf{J} . Such a comparison may provide further insight into the influence of planar components of current (generated by the Hall term) on the reconnection rate.

Acknowledgements. This work was part-funded by the RCUK Energy Programme under grant EP/I501045 and the United Kingdom Engineering and Physical Sciences Research Council through a CASE studentship. JT would like to thank T. Neukirch (University of St Andrews) and J. McLaughlin (University of Northumbria) for helpful discussions. IDM acknowledges support of a Royal Society University Research Fellowship.

References

- Arber, T. D., Longbottom, A. W., Gerrard, C. L., & Milne, A. M. 2001, *Journal of Computational Physics*, 171, 151
- Aschwanden, M. J., Fletcher, L., Schrijver, C. J., & Alexander, D. 1999, *ApJ*, 520, 880
- Ben Ayed, N., McClements, K. G., & Thyagaraja, A. 2009, *Journal of Plasma Physics*, 75, 203
- Birn, J., Drake, J. F., Shay, M. A., et al. 2001, *J. Geophys. Res.*, 106, 3715
- Birn, J. & Priest, E. 2007, *Reconnection of Magnetic Fields* (New York: Cambridge University Press), 94–95
- Biskamp, D. 2000, *Magnetic Reconnection in Plasmas* (Cambridge University Press)
- Bulanov, S. V. & Syrovatskii, S. I. 1980, *Soviet Journal of Plasma Physics*, 6, 1205
- Craig, I. J. D. & Litvinenko, Y. E. 2002, *ApJ*, 570, 387
- Craig, I. J. D. & Litvinenko, Y. E. 2008, *A&A*, 484, 847
- Craig, I. J. D. & McClymont, A. N. 1991, *ApJ*, 371, L41
- Craig, I. J. D. & McClymont, A. N. 1993, *ApJ*, 405, 207
- Craig, I. J. D. & Watson, P. G. 1992, *ApJ*, 393, 385
- Craig, I. J. D. & Watson, P. G. 2005, *Physics of Plasmas*, 12, 012306
- De Moortel, I. 2005, *Royal Society of London Philosophical Transactions Series A*, 363, 2743
- Dorelli, J. C. 2003, *Physics of Plasmas*, 10, 3309
- Gallagher, P. T. & Long, D. M. 2011, *Space Sci. Rev.*, 158, 365
- Hassam, A. B. 1992, *ApJ*, 399, 159
- Haynes, A. L. & Parnell, C. E. 2007, *Physics of Plasmas*, 14, 082107
- McClements, K. G., Shah, N., & Thyagaraja, A. 2006, *Journal of Plasma Physics*, 72, 571
- McClements, K. G., Thyagaraja, A., Ben Ayed, N., & Fletcher, L. 2004, *ApJ*, 609, 423
- McLaughlin, J. A., De Moortel, I., Hood, A. W., & Brady, C. S. 2009, *A&A*, 493, 227
- McLaughlin, J. A. & Hood, A. W. 2004, *A&A*, 420, 1129
- McLaughlin, J. A. & Hood, A. W. 2005, *A&A*, 435, 313
- McLaughlin, J. A. & Hood, A. W. 2006, *A&A*, 452, 603
- McLaughlin, J. A., Hood, A. W., & de Moortel, I. 2010, *Space Sci. Rev.*, 62
- Nakariakov, V. M., Ofman, L., Deluca, E. E., Roberts, B., & Davila, J. M. 1999, *Science*, 285, 862
- Nakariakov, V. M. & Verwichte, E. 2005, *Living Reviews in Solar Physics*, 2, 3

- Ofman, L., Morrison, P. J., & Steinolfson, R. S. 1993, ApJ, 417, 748
- Ofman, L. & Wang, T. J. 2008, A&A, 482, L9
- Priest, E. & Forbes, T. 2007, Magnetic Reconnection: MHD Theory and Applications (Cambridge University Press)
- Senanayake, T. & Craig, I. J. D. 2006, A&A, 451, 1117
- Threlfall, J., McClements, K. G., & de Moortel, I. 2011, A&A, 525, A155+
- Wang, T. J. & Solanki, S. K. 2004, A&A, 421, L33